Structure and magnetism of new hybrid cobalt hydroxide materials built from decorated brucite layers†

Tony D. Keene, Mark E. Light, Michael B. Hursthouse and Daniel J. Price*

Graphical Abstract

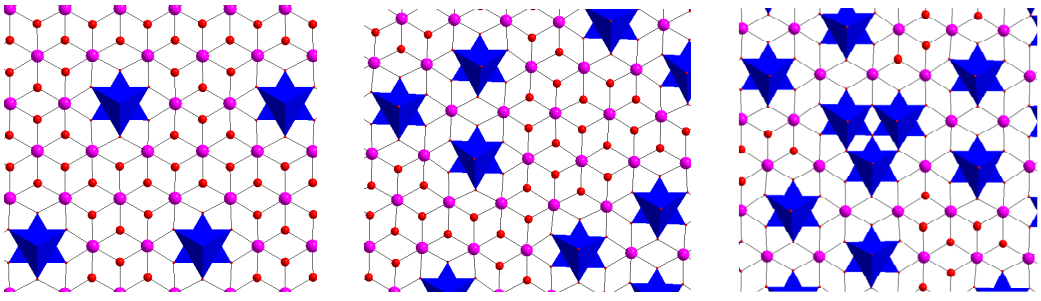

Magnetic ordering is seen in two new trigonally symmetric pseudo-two-dimensional complex cobalt hydroxides, which have a characteristic $1/9^{th}$ and $3/19^{th}$ site depletion.

Structure and magnetism of new hybrid cobalt hydroxide materials built from decorated brucite layers†

Tony D. Keene,[a,c] Mark E. Light,[b] Michael B. Hursthouse[b] and Daniel J. Price*[a]

[a] WestCHEM, School of Chemistry, University of Glasgow, Glasgow, G12 8QQ, United Kingdom. E-mail: Daniel.Price@glasgow.ac.uk; Fax: +44-141-330-4888

[b] School of Chemistry, University of Southampton, Highfield, Southampton, SO17 1BJ, United Kingdom.

[c] Present address: School of Chemistry, Building F11, University of Sydney, Sydney, NSW 2006, Australia.

* E-mail: Daniel.Price@glasgow.ac.uk

† Electronic supplementary information (ESI) available: Trigonally symmetric site depleted triangular lattices, infrared spectra, a.c. magnetic susceptibility measurements and magnetic phase diagram, coupling scheme and schematic representations of the magnetic ground states of **1**. CCDC references numbers 275122 (**1**), 275671 (**2**) and 219800 (**3**). For ESI and crystallographic data in CIF format see DOI: xxxxxxx.

The structure, synthesis and magnetic properties of three new complex cobalt hydroxyl oxalates are presented, showing a modification of the 2-D double layer hydroxide structure. $Co_{12}(OH)_{18}(ox)_3(pip)$ [ox = oxalate, $C_2O_4^{2-}$; pip = piperazine, $C_4N_2H_{10}$] (**1**), is essentially built from brucite-like layers with a *one ninth* depletion of the octahedral sites and a preservation of a trigonal crystallographic symmetry. $ACo_{28}(OH)_{43}(ox)_6Br_2(H_2O)_2$ [A = Na (**2**), K (**3**)] are similarly composed of a brucite-like layer with *three nineteenths* depletion of octahedral sites, again preserving a trigonal symmetry. Both **2** and **3** show a small degree of structural disorder within the framework. All of these compounds have alternating layers of a mineral-like metal hydroxide structure and a metal oxalate coordination network, with the depletion in the hydroxyl layers being templated by the coordination network. Magnetic studies of **1** reveal a metamagnetic character, with the onset of an antiferromagnetic phase

below T_c = 23.5 K (H = 0 G), and a first order antiferromagnet to metamagnet transition at H_c = 500 – 1000 G (T = 20 – 6 K). Compound **3** shows a more conventional ferrimagnetic ordering below 33(±1) K with a small coercive field of 107(±5) G at 10 K.

Introduction

The properties of all functional electronic materials are determined by their composition and their structure. It is an ultimate goal for materials scientists to form new materials with such precise structural control as to give completely predictable electronic properties. Fortunately this ambition remains largely beyond our grasp, allowing synthetic chemists the frequent pleasure of surprise in what they may make. However, there are many important structural features which are amenable to some level of control such as the characteristic dimension of a material which has implications for many physical properties. One way to control dimensionallity is to build materials from components with different characters, typically in which the nature of electron-electron interactions varies greatly, and in which it is possible to physically segregate these parts on a microscopic level. Such a spatial confinement can be achieved in *composite* or *hybrid* materials in which characteristic "organic" and "inorganic" parts are well separated.[1] This is one reason for the current interest in metal-organic frameworks (MOF's).[2] In magnetic materials it is not only the dimensionality[3] of the coupled network, but also the specific network topology and the strength and sign of all coupling interactions that are key to the nature of any cooperative magnetic behaviour.[4]

The family of double layered hydroxides are a very important group of structures both scientifically and commercially. They are based upon the brucite structure of $Mg(OH)_2$, which has very strong intralayer interactions and much weaker interlayer interactions, as evidenced by the capacity of members of this family to intercalate small molecules, swelling the interlayer separation.[5] Structural modifications come in a number of varieties:

i) the hydroxyl group can be replaced by some other type of ligand capable of a μ^3-bridging coordination. Examples range from alkoxides,[6] to the exchange for an

oxygen atom from a $[(Si_2O_5)_n]^{2n+}$ silicate layer, as seen in the smectite mineral group.[7]

ii) The M^{II} can be replaced by a M^{III} ion, which is coupled to the incorporation of a charge balancing anion in the interlayer space. Hydrotalcite; $Mg_6Al_2(OH)_{16}(CO_3)(H_2O)_4$ is a proto-typical mineral in this family,[8] but its is also possible to form all sorts of variants including the incorporation of metal *tris*-oxalate counter ions.[9]

iii) A third family is created by the removal of some M^{II} ions. In this case it is very common for the vacancy to be decorated by a tetrahedral coordinated M^{II} ion on either side of the layer. This is the case for a small group of basic zinc hydroxide minerals, including; namuwite[10] and ramsbeckite,[11] and an increasing number of complex cobalt hydroxides.[12-17]

From a magnetic perspective the brucite structural family offer an interesting prospect to find exotic new behaviour. In brucite itself the metal ions are arranged in a triangular lattice, and site substitution, or depletion, that preserves a trigonal symmetry can result in other potential geometrically frustrated networks.[18] In fact it is only possible to construct trigonally symmetric super-cells that include; 3, 4, 7, 9, 12, 13, 16, 19, ... lattice points from the original triangular net.[19] These Löschian numbers are given by the formula ($a^2 + ab + b^2$). Thus a $^1/_3$ site depletion gives a honeycomb net; a $^1/_4$ site depletion gives the kagomé net (Fig. 1 a); $^1/_7$ the maple leaf net (Fig. 1b), and so on. The first members of this series of trigonally symmetric networks are shown in ESI Figure S1. Although trigonal symmetry can be important for 2-D spin frustration, it is not a guarantee of a non-bipartite lattice.

The type of magnetic behaviour seen in these site depleted triangular lattice materials depends upon the nature of all the coupling interactions. Antiferromagnetic couplings within a layer can result in 2-D spin frustrated behaviour, with strongly non-colinear ground state configurations. However, some ferromagnetic intralayer interactions can result in ferri- or ferro-magnetic intralayer order. In these cases the nature of the interlayer interaction is crucial to the ground state configuration. If positive we expect an overall ferri- or ferromagnetic ground state, if negative we expect an antiferromagnetic ordering, with transition to a metamagnetic state above some critical field, H_c.[20]

We present here the synthesis, structure and magnetism, of three new complex cobalt hydroxide oxalates. Compound **1**, $Co_{12}(OH)_{18}(ox)_3(pip)$ [ox = oxalate, $C_2O_4^{2-}$; pip =

piperazine, $C_4N_2H_{10}$] has a $1/9^{th}$ depleted structure and shows an antiferromagnetically ordered ground state, with a field induced metamagnetic phase. Compounds **2** and **3** have idealised compositions $ACo_{28}(OH)_{43}(ox)_6Br_2(H_2O)_2$ [A = Na (**2**); A = K (**3**)] and show a $3/19^{th}$ depleted structure. The magnetism of **3** shows a long range ferrimagnetic ordering below 33(±1) K.

Results and Discussion

Synthesis

All three compounds (**1**, **2** and **3**) have very low ambient solubility in water. A fact that is not surprising given their extended network structures. They are all formed by hydrothermal crystallisations at 225 °C and above, as are a number of competing phases, which contaminate the products and must be removed either manually or by other physical methods. Much effort has been directed at optimising the synthesis, and yields of the products have been improved, but it is evident that even in these chemically simple systems, there are many complex equilibrium and control of the solution species is not at all trivial. The synthesis of these compounds are neither straightforward chemical transformation nor "molecular" crystallisation, where there is a close correspondence between solution and solid-state species. Given their structures it is clear that their formation through crystallisation must involve a large number of surface processes and a very good control of both kinetic and thermodynamic aspects in the crystallisation regime is required to fully optimise their synthesis.

In the case of **1** $Co_{12}(OH)_{18}(ox)_3(pip)$ we can obtain a high yield of thin blue hexagonal plates, but a significant contamination from the hydroxyl oxalate; $Co_2(OH)_2(ox)$ is observed.[21]. This particular impurity (larger maroon crystals) is rather robust, but can be separated in a number of ways, including sieving to differentiate on particle size. The synthetic conditions are more basic than required for the related phase $Co_7(OH)_8(ox)_3(pip)_6$.[22] The discovery of **2** and **3** came out of an exploration of cobalt oxalate phases that can be produced from solutions containing very high concentrations of alkali metal salts. We have previously reported[23] the synthesis of $Na_2Co_2(ox)_3(H_2O)_2$ from hydrothermal solutions with very high Na^+ concentrations. Typically $Na_2Co_2(ox)_3(H_2O)_2$ could be made cooling a mixture of

$CoCl_2$, Na_2ox, NaCl and H_2O in 1:3:40:200 proportions, from 225 °C. Compound **2** was first discovered as a very minor impurity in a similar reaction where NaCl is replaced by NaBr. Such reactions produce a mixture of three solids: recrystallised NaBr (~10 g), $Na_2Co_2(ox)_3(H_2O)_2$ (~100 mg) and **2** (~1 mg). Importantly **2** is not formed from the chloride solutions giving some evidence of the importance of the bromide ion in the synthesis. Attempts to optimise the synthesis result only in modest improvements in yield. A re-visitation of the related reaction system[24] where $CoCl_2$, K_2ox, KBr and H_2O are mixed in proportion 1:2:100:460 to produce $K_2Co(ox)_2$ revealed a few thin blue hexagonal plates of **3** as a very minor "impurity" phase. Adjusting the synthetic conditions proved more fruitful and the yield of **3** was increased from a few crystals to an extractable and manageable quantity (~10 mg). We believe that there may be a correlation between the "ease of synthesis" and the role of the Na^+ and K^+ cation in the respective structures.

Crystal Structures

The structures were determined by single crystal X-ray diffraction. See Table 1 and Experimental Section for measurement, solution and refinement details.

Structure of 1.

The compound $Co_{12}(OH)_{18}(ox)_3(pip)$ (**1**) crystallises in the trigonal space group $P\bar{3}$ (# 147) and consists of two types of alternating layers (Fig. 2): type 1, cationic layers of cobalt hydroxide with the formula $[Co_{10}(OH)_{18}]_n^{2n+}$ and type 2, an anionic coordination network, $[Co_2(ox)_3]_n^{2n-}$ with the honeycomb motif. The structure of the type 1 layer is based upon the brucite structure, as seen in β-$Co(OH)_2$. This consists of a double layer of close packed hydroxide ions with metal ions on every octahedral site, resulting in layers of edge shared MO_6 octahedra. Thus each hydroxide ions is μ^3-bridging and the OH bond vector is normal to the layer. In **1** the type 1 layer has essentially the brucite structure with a periodic defect; *one out of* every *nine* of the octahedral cobalt sites is vacant. Giving the network shown in Figure 1c. This vacancy is decorated above and below by tetrahedrally coordinated cobalt(II) ions. Thus the triangular faces of the octahedral cage of oxygen atoms form the base of the CoO_3N polyhedra. Adjacent type 1 layers are bound together through a bridging piperazine molecule which links apical sites of the tetrahedrally coordinated Co(II)

ions, being threaded through the holes in the cobalt oxalate honeycomb network. The piperazine adopts a chair conformation and is disordered on a three-fold symmetry axis. Examination of short contacts reveals hydrogen-bonding between these ionic layers (Table 2, Fig. 2c). There are three crystallographically independent hydroxide ions. Two of which are μ^3-bridging to three octaheadrally coordinated cobalt ions and these also form short approximately linear hydrogen-bonds to oxygen atoms in the $[Co_2(ox)_3]_n^{2n-}$ network. The third hydroxide; O(1) is μ^3-bridging to two octahedrally coordinated Co ions and one tetrahedral ion, it is angled at ~30 ° to the layer normal, and is only weakly involved in hydrogen bonding. There are no interactions for the amine proton with the nearest potential hydrogen bond acceptor at a distance of 4.13(1) Å.

The 2-D Co(II) oxalate honeycomb network has been seen previously in $Co_2(ox)_3(C_{28}N_6H_{20})$.[25] This network is distorted from an ideal trigonal symmetry, as is commonly seen in other transition metal oxalate materials [26]. Analysis of the Co(II)-ox-Co(II) separation (d_1) from structures deposited in the Cambridge Structural Database[27] gave a mean value of 5.46 Å which compares well with the value of 5.440(1) Å obtained from **1**. The Co···Co separation (d_1) ideally produces a 2-D cell parameter $a = d_1\sqrt{3}$, which is seen to match very well the ideal cobalt hydroxide supercell of 9.504 Å (three times the *a*-parameter [28] of β-$Co(OH)_2$). Clearly the close match in lattice parameters, the complimentary charge density of the alternating layers and the hydrogen-bonding interactions all conspire to stabilize the formation of this hybrid material. We view the type 1 layers as being templated by the type 2 coordination network.

Structure of 2 and 3.

Compounds **2** and **3** are essentially isomorphous and isostructural crystallising in the polar trigonal space group *P*31*c* (# 159). The difference between the compounds is the alkali metal cation (Na in **2**, K in **3**), differences in crystal quality result in small differences between refined models (see Experimental Section). We describe the structure of **2** and give comparable details for **3** in square brackets. The structure of **2** [**3**] has great similarity to that of $[KCo_{14}O(OH)_{21}(ox)_3]$ recently reported by Zhang.[17] The precise formulation of **2** [**3**] is quite difficult to determine. From the X-ray data we refine a composition of $NaCo_{28.29}Br_{2.16}C_{12}H_{48.27}O_{69.86}$

$[KCo_{28.18}Br_{1.95}C_{12}H_{47.89}O_{69.65}]$ which is consistent with both EDX and C, H microanalysis. The non-stoichiometric formula is a result of disorder at a number of sites. We describe the idealised (non-disordered) structure first, which we refine as greater than 90% of the phase, and then talk about the disorder as deviations from this structure. Thus an idealised (non-disordered) composition of **2** [**3**] is $ACo_{28}(OH)_{43}(ox)_6Br_2(H_2O)_2$. where A = Na [K]. As suggested by the empirical formula and the large unit cell volume, the structure is complex. The asymmetric unit comprises of ten cobalt atoms of which eight are in CoO_6 octahedral environments and two have a tetrahedral CoO_4 geometry. Collectively these cobalt ions are coordinated by are two crystallographically distinct oxalato ions and fifteen bridging hydroxyl groups. In addition there are two main bromide ion sites and one sodium [potassium] ion; all of which lie along the three-fold axis. Overall the structure is comprised of a three dimensional cobalt-hydroxide network, however there is a strong 2-D character to this material, with many structural similarities to **1**. We see an alternation of two types of layer: type 1 a metal hydroxide layer with the composition $[Co_{22}(OH)_{37}]_n^{7n+}$ and type 2, essentially a layer of a coordination network with the formula $[Co_6(OH)_6(ox)_6]_n^{6n-}$ having interstitial Na^+ [K^+] and Br^- ions to preserve electroneutrality (Fig. 3).

As with **1**, the cobalt/hydroxide layer (type 1) is based on the brucite structure, although here we see a periodic loss of *three out of* every *nineteen* cobalt ions from the octahedral sites within the layer, giving the network structure shown in Figure 1d. These layer defects occur in groups of three centred about the three-fold crystallographic axis at ($^1/_3$, $^1/_3$, *c*). The remaining octahedral cage of oxygen atoms forms the basal set for two tetrahedrally coordinated cobalt ions, which decorate the layer (Fig. 3b). The apical hydroxide of the CoO_4 tetrahedra is μ^3-bridging two further Co^{2+} ions within the type 2 layers (Fig. 3c). By linking cobalt in both layer types, these tetrahedra connect all cobalt ions into a 3-D cobalt hydroxide network.

The type 2 (oxalate containing) layers comprise of *bis*-hydroxyl bridged, '$Co_2(OH)_2$' units which are then linked together into an essentially honeycomb network by four bridging and chelating oxalate ions. Thus each cobalt is coordinated by two oxalate ions in a *cis*-geometry and two hydroxide ions. This rather odd honeycomb-like net that forms the type 2 layer contains three distinct trigonally symmetric “cavities”, labelled A, B and C (Fig. 3c). The two smaller holes; B and C have well defined

contents. Hole B contains a bromide ion, Br(1) with a 96.3(8) [86.9(10)] % occupancy, and hole C contains both a bromide ion, Br(2) with 93.5(8) [89.0(9)] % occupancy and the alkali metal at 100 % site occupancy. Each bromide ion is hydrogen-bonded to hydroxyl groups in the structure (Fig. 4, Table 3). In addition Br(2) forms an ion pair with the alkali metal ion; Br–Na 2.989(9) [Br–K 3.048(5)] Å. Both of the bromide ions sit in the trigonal cluster of tetrahedral Co(II) ions and through hydrogen bonding interactions locally template the formation of this part of the cobalt hydroxide structure. It is interesting to note that the bromide ion is an essential component of the synthesis, and that no such material has ever been seen when Br is substituted for Cl in the synthesis. The structural description so far constitutes the main part of the structure of **2** [and **3**]. However careful crystallographic refinement reveals further significant anomalies in the residual Fourier difference maps due to structural disorder of the framework.

Disorder in the structure of 2 [and 3].

All of the disorder in the structure is centred along the three-fold axis passing through the larger hole A, at (0, 0, *c*). The components of this disorder are shown in Fig. 5. Just off this axis lies Co(8), which has a refined occupancy of 89.8(3) [94.0(2)] %. The trigonal symmetry creates a triangle of Co(8) coordination polyhedra, that all share the hydroxyl group, O(18) and its symmetry equivalents (Fig. 5a). In this region of the structure we find a number of significant peaks in the Fourier difference map. There are two nearby peaks on the trigonal axis, which corresponds to essentially monatomic μ^3-bridging species. After much consideration we assign one of these as a bromide; Br(3) (Fig. 5b) with a 25.6(14) [19.4(14)] % occupancy and the other as an oxygen; O(24) (Fig. 5c), probably a hydroxide ion with a 45(3) [41(2)] % probability of occupancy. This must mean that for some of the time when Co(8) is present there must be a ligand vacancy at this 3-fold site, and the Co(8) ions will have a square based pyramidal coordination (Fig 5a). In addition we see peaks in the Fourier difference map that correspond to a 'decoration' of the Co(8) vacancy, with tetrahedrally coordinated cobalt ions Co(8A) and Co(8B) (Fig. 5d), on either side of the brucite-like layer (much like the layer decoration described in the main part of the structure). The occupancy of these tetrahedral ions (10.2(3) [6.0(2)] %) is constrained to be equal to the probability of vacancy at the Co(8) site. From a structural

perspective, it seems most likely that Co(8) vacancies are not entirely random, but occur in a cluster of three, about the trigonal axis. The decoration of the vacancies results in two different types of tetrahedral metal ion clusters on the different faces of the layers. In this polar space group the positions of these two cluster types help to reveal an obvious polarity. Thus, on one side, three Co ions each share two verticies to form a ring (Fig. 6). On the other side of the layer the coordination sphere of the Co_3 unit contains a single central μ^3-bridging hydroxyl group (Fig. 6), which lies at the O(24) site. [Note: the O(24) occupancy is greater than the probability of Co(8) site vacancy, and so an oxygen atom exists on approximately the same site for the two different structural scenarios (Fig. 5c and 5d).] The apical coordination of Co(8A) and Co(8B) is achieved by fixing O(27) and O(28) in idealized geometries. The only remaining significant peaks in the Fourier difference maps appear near the middle of the void space; A (see Fig. 3c). While it is likely that there are water molecules in this space, they are not well defined, with large thermal parameters. From symmetry considerations these two sites (O(25) and O(26)) must be no more than one third occupied and are constrained to equal this value in the model.

Magnetism

The magnetism of derivatives of these so-called double layered cobalt hydroxides has received much attention. As with these related compounds,[12-17] we expect the tetrahedrally coordinated ions to form a $^4A_1$ ground term, and the octahedrally coordinated Co(II) ions to adopt a $^4T_{1g}$ spin configuration. Although the orbital contribution to the momentum are likely to produce local spin anisotropies, exactly how these individual ion properties will contribute in the bulk magnetic behaviour is difficult to predict. Since these are insulating phases super-exchange interactions will dominate. In general large exchange interactions are associated with shorter bridging pathways, we expect the magnetism to be dominated by in-plane, hydroxyl bridged coupling interactions. It is also important to place these materials in the context of other two dimensional materials, and to highlight the importance of the trigonal symmetry. The triangular lattice with antiferromagnetic interactions while subject to the effects of geometric spin frustration, does posses a long range ordered ground state. The effect of a periodic site depletion is to reduce the connectivity. The $^1/_4$ depleted triangular lattice, a.k.a. the kagomé net (Fig. 1a), show extreme geometric

spin frustration if the nearest neighbour interactions are antiferromagnetic, and does not posses a conventionally ordered ground state. Calculations on the 1/7th depleted, maple leaf net (Fig. 1b) suggest an ordered ground state.[29] Such spin frustration is only observed when all coupling interactions are of equal strength and negative sign. In the present case inequalities in coupling strength and the possibility of ferromagnetic interactions are more likely to result in ferrimagnetic ordering.

Magnetism of 1.

D.C. measurements.

Field cooled magnetisation (FCM) (H = 200 G) of **1** shows the susceptibility to increase on cooling reaching a sharp maximum at 24.1(±0.3) K, before decreasing and tending to a value of $\chi_{(T = 0K)}$ ~ 0.42 cm^3 mol^{-1} (Fig. 7a). Above 90 K, the sample shows Curie-Weiss behaviour, with C = 2.63(3) cm^3 mol^{-1} K (where mole^{-1} is per mole of Co ions) and θ = -3.6(16) K (Fig. 7a). This corresponds to an average moment of 4.59 μ_B per Co ion, and assuming all Co(II) are $S = {}^3/_2$ ions, we calculate an average g-value of 2.37. The negative Weiss constant is consistent with the presence of antiferromagnetic interactions and the cusp in the susceptibility indicates a magnetic phase transition to an ordered antiferromagnetic state. We determine T_c = 23.5(±0.5) K, as the steepest part of the $\chi T(T)$ curve. A reasonable starting point for the description of magnetism in 3-D structures is mean field theory (MFT), which predicts $|\theta/T_c = 1$. Commonly materials are characterised by a ratio $|\theta/T_c > 1$, when the suppression of long-range magnetic ordering is often attributed to either low-dimensional character, or to spin frustration within the material. For **1** we obtain $|\theta/T_c$ = 0.15. While it is generally the case that θ is roughly proportional to J, in this case we expect to have a number of different coupling interactions; including both strong ferro- and strong antiferromagnetic interactions, which must conspire to produce a very small value of θ. Another prediction of MFT is that $\chi_{(T=0)}/\chi_{(T=Tc)} = {}^2/_3$. The large observed deviation; $\chi_{(T=0)}/\chi_{(T=Tc)}$ = 0.28, suggests a more complex behaviour. Isothermal magnetisation measurements (Fig. 7b) reveal qualitatively different behaviour for data above T_c (25 and 30 K) compared to measurements below T_c (6, 15 and 20 K). For $T < T_c$ we see a field induced magnetic phase transition, typical of a metamagnet. At low fields the sample behaves as an antiferromagnet with a small value for the gradient dM/dH. Above the critical field we see a much steeper rise in

M, with a gradient typical of a ferromagnetic-like state. The critical field can be determined as the peak maximum in the susceptibility plot; d*M*/d*H* verses *H* (Fig. 7b insert).

The saturation magnetisation of the sample is also quite revealing. Even at the lowest temperatures (6 K) with the highest field (50 kG) we do not reach the asymptotic saturation value. However extrapolation suggest M_{sat} ~ 5.0(±0.3) kG cm^3 mol^{-1} (per mole of Co ions). This corresponds to about one quarter the value expected for a ferromagnetic alignment of all Co ion moments (calculated using the average g-value determined from the high temperature susceptibility data).

Hysteresis measurements at 6 K, between ±50 kG, show a classic metamagnetic profile (Fig. 7c). There is some hysteresis involved in overcoming the weak antiferromagnetic interaction, consistent with a first order magnetic phase transition. The derivative curve (Fig. 7c insert) shows a shift of ~400 G in the transitions between the two directions of travel (*H* increasing *vs H* decreasing). We observe a remnant magnetisation of 240 G cm^3 mol^{-1} (*H* = 0 G), with a corresponding coercive field of 390 G.

A.C. measurements and magnetic phase diagram.

A series of a.c. magnetic susceptibility measurements were performed as a function of temperature and d.c. offset field. The data for experiments in the range H_{dc} = 0 – 800 G and *T* = 5 – 40 K (with H_{ac} and ω fixed at 3.5 G and 103 Hz respectively) are shown in Fig. 8a and 8b. The temperature dependence of the real component of the a.c. susceptibility changes quite significantly as a function of d.c. offset field. On increasing the field we note

i) a shift in the peak position to lower temperatures

ii) the peak height increases (reaching a maximum at H_{dc} = 500(±50) G) before decreasing with further increase in H_{dc}.

iii) We also see a significant change in the peak shape, with a general broadening at high d.c. fields.

The temperature dependence of the imaginary component of the a.c. susceptibility shows even greater changes for increasing offset field. At offset fields of $H_{dc} \leq 300$ G, only very small values of χ'' are observed. At H_{dc} = 400 G we see a massive change in $\chi''(T)$, with the formation of a large peak (maximum at 21.7(±0.3) K). Further increases see a maximum peak height for H_{dc} = 500(±50) G before decreasing.

Alongside this we again see a change in the peak shape with a broadening on the low temperature side of the maximum, and the formation of a shoulder on the high temperature side at ~26 K.

The real part of the susceptibility is simply the gradient of the $M(H)$ curve at the temperature of the experiment. The a.c. experiment provides a much more precise determination of this value compared to a direct measurement of M. Consequently, for an antiferromagnet to paramagnetic phase transition, basic thermodynamics tells us we can take the ordering temperature, T_c to be the point of the steepest gradient in the $\chi T(T)$ curve. The imaginary component of the susceptibility, the out-of-phase component, is proportional to the work done on the sample. It is zero for both paramagnets and antiferromagnets, but non-zero for materials with a net magnetisation such as; ferromagnets, ferrimagnets, spin glasses, and superparamagnets below a blocking temperature. The plot of $\chi''(\chi')$ for different values of ω and T (Fig. S2 in ESI) clearly indicates the formation of a long range ordered magnetic state. Conventionally, the transition to form a paramagnetic state to a magnetically ordered state with a net moment is marked by a non-zero value for χ'' for $T < T_c$. It is often the case that $\chi''(T)$ shows a maximum, especially for hard magnetic systems. The antiferromagnet to metamagnet phase transition occurs at a critical field, H_c applied along the axis of the spin moments. In a powder sample with a random distribution of particle orientations, it is the component of the field along this axis that is required to drive the phase transition. Thus initially as the field is increased only a small proportion of the sample has an orientation, which allows $H_{||c\text{-}axis} > H_c$

The magnetic phase diagram (H, T) for **1** is dependant on the relative orientation of H to the crystallographic c-axis. This is not easily measured without a large single crystal of the compound. Nevertheless we can extract a semi-quantitative diagram from power magnetisation measurements. As the response is dominated by components of the sample when H is parallel to the c-axis. (See figure S3 in ESI).

Magnetostructural considerations.

The structure of **1** can be broken down into seven important exchange interactions: J_1, J_2 and J_3 describe the coupling interactions in the cobalt hydroxide net formed from the octahedrally coordinated Co^{II} ions in the type 1 layer (Fig. 9a). J_4 connects the

tetrahedreally coordinated ions to the octahedreally coordinated ions. J_5 connect Co^{II} ions within the type 2 layer into a 2-D honeycomb network. We also consider two types of potential interactions between layers: J_6 is the interaction between type 1 and type 2 layers. J_7 represents the interaction between adjacent type 1 layers, mediated between tetrahedrally coordinated Co ions that are bridged by the piperazine molecule. $J_{1\text{-}4}$ are hydroxyl bridged pathways and are likely to form the dominant exchange interactions. J_5, the oxalate mediated exchange pathway for which we can expect a coupling ($2J$) of -18(±3) K for Co^{II} ions.[23, 24, 30] In comparison with the other interactions in this structure J_6 and J_7 must be much weaker, as no bonded pathway exists to form J_6, and J_7 corresponds to two Co^{II} ions being bridged by a piperazine (*i.e.* a 5 bond coupling interaction through a saturated organic ligand). We expect the observed magnetism to be dominated by the behaviour of the type 1 layer (more spin moments, stronger couplings). For coupling interactions $J_{1\text{-}4}$ we can consider the magnetic ground state structure for positive (ferromagnetic) and negative (antiferromagnetic) (Table S1 in ESI). We expect a degree of spin frustration in 12 out of the 16 possible ground states. The non-frustrated ground states all have a net moment (Fig. S5 in ESI). These include: the ferromagnetic structure, where $J_{1\text{-}4}$ are all positive [(J_1, J_2, J_3, J_4) = (+, +, +, +)]. This corresponds to 10 out of the 12 Co ions in the formula unit contributing to the sample magnetisation (The cobalt ions in the type 2 layer, have never been observed to have a mutually parallel alignment for a bridging oxalate.) The (+, +, +, –) and the (–, +, +, +) configurations have 6 out of the 12 Co being non-compensated, while the (–, +, +, –) configuration would have only 2 out of 12 of the Co ions contributing to the sample moment. Using the average g-value obtained from high temperature data, we expect a saturation magnetisation of 19855 (for 12/12 uncompensated moments), 16545 (10/12), 9927 (6/12) and 3309 (2/12) G cm^3 mol^{-1}. This simplified approach makes no account for the different moments for different ions. But typically octahedrally coordinated high-spin Co(II) have larger orbital contributions than tetrahedrally coordinated Co(II), and thus we would expect a saturation magnetisation for the (–, +, +, –) structure (Fig. 9b) to be greater than 3309 G cm^3 mol^{-1}. From the observed value of M_{sat} ~5000 G cm^3 mol^{-1}, and in the absence of any evidence of spin frustration, we suggest that the (–, +, +, –) spin configuration is the ground state for the type 1 layer. At low fields, adjacent type 1 layers have opposite spin orientations (*i.e.* $J_7 < 0$), which means that the internal

(dipolar) field at the Co site in the type 2 layer is exactly zero in the ground state. It only requires a weak field to overcome the small negative coupling J_7, and to flip the spin configuration, so that adjacent type 1 layers have the same relative spin orientations.

Magnetism of 3.

At high temperatures the susceptibility of **3** shows field independent behaviour characteristic of a paramagnetic state. Above 120 K the sample obeys Curie-Weiss law, with C = 5.5(1) cm^3 mol^{-1} K (where mol^{-1} is: per mole of Co ions); θ = -177(8) K (Fig. 10a). At low temperatures the susceptibility increases. The sample develops a field dependent spontaneous moment below the transition at 33(1) K (the maximum gradient), corresponding to long-range magnetic order below this temperature. Field dependent measurements at 10 K reveal a hysteresis curve (Fig. 10b) typical of a soft magnetic state, with a remnant magnetisation of 373(5) G cm^3 mol^{-1} and a coercive field of 107(5) G. The large negative Weiss constant is a clear indication of the dominant antiferromagnetic exchange processes in **3**. The observation of a spontaneous moment must be associated with an ordered spin configuration where the vector sum of individual moments does not cancel. This suggests either ferrimagnetism or spin canted antiferromagnetism. The sigmoidal shape of the hysteresis curve, particularly the linear variation in M at high field also supports this ferrimagnetically / canted antiferromagnetically ordered hypothesis. The intercept of the liner fit to the high field data with the ordinate-axis gives a saturation magnetisation for the magnetically ordered structure. We calculate M_{sat} = 2037(7) G cm^3 mol^{-1}, which corresponds to approximately 12% of the magnetisation of a ferromagnetic structure. Although this magnetisation corresponds to a spin configuration where 24 of the 28 Co ions aligned with spins antiparallel and the remaining 4 having parallel moments, the complexity of this material with ten crystallographic independent Co^{2+} ions linked by 21 distinct μ-OH superexchange pathways, warrants much caution. In addition the structure shows a profound 2-D character and is potentially highly spin frustrated. This may well be reflected in the high ratio of $|\theta|/T_c$ (= 5.38).

Conclusions

We report three new materials with strongly 2-dimensional structures, in which we see a decoration of a brucite lattice structure. This decoration preserves a crystallographic trigonal symmetry, with implications for spin frustrated materials. In **1** the $1/9^{th}$ site depletion is the first time that this stoichiometry is reported. The fact that we can make **1** in high yield is evidence of the stability of the phase, in which there is a good electrostatic match between the coordination network part and the metal hydroxide part giving rise to a templating effect in the synthesis. Indeed the hydrogen bonding capacity of the brucite layers to match the metal oxalate framework is supported by the intercalation studies of metal *tris*-oxalates into brucite like layers.[9] In **2** and **3** we see the $3/19^{th}$ depleted structure related to that of Zhang et al.[17]. It is a pleasant surprise that such a structurally complex material can be formed from simple mixtures of $CoCl_2$, $Na_2C_2O_4$ [or $K_2C_2O_4$] and NaBr [or KBr] in water. In these materials we are able to model the significant structural disorder within the framework. Magnetically **1** shows an ordered antiferromagnetic structure at low temperatures in zero applied field, but above a small critical field a large moment develops, revealing a metamagnetic transition. A simple analysis suggests the same local spin state configuration in the vicinity of the octahedral vacancy as has been observed in the related materials cobalt hydroxides; with $1/4^{th}$ [12,13], $1/7^{th}$ [16] and $3/19^{th}$ [17] site depleted layers. The low value of the critical field for the transition to a metamagnetic state is good evidence of a very weak antiferromagnetic interlayer interaction. In **3** we see the formation of a ferrimagnetically ordered state below 33(±1) K, with much similarity to that reported for $[KCo_{14}O(OH)_{21}(ox)_3]$ by Zhang.[17] There is no doubt that the structural complexity of **3** will make a complete understanding of its magnetic properties very challenging. Together these compounds extend the family of known materials derived from a decorated brucite structure. The preservation of trigonal symmetry while aesthetically pleasing is only likely to be important with regard to spin frustration in other derivaties of these materials. The observed structures are directly related to the templating effects of both the coordination networks and interstitial ions. These inform our general understanding of local and global structures in the family of double layered hydroxides, and reinforce the vital role of anion templating of local defects from an idealised brucite structure.

Experimental Section

Synthesis

General aspects.

All reagents had a minimum 99 % purity and were obtained commercially and used as received, without further purification, with the exception of piperazinium bis(hydrogen oxalate) {[pipH_2][ox$H$]$_2$} which can be prepared by literature methods.[31] Hydrothermal reactions were performed in 23 mL capacity Parr Teflon lined acid digestion bomb model 4749. C and H analysis was obtained using an Exeter Analytical Inc. CE-440 Elemental Analyser. Infrared spectra were obtained on a Perkin Elmer Spectrum One FTIR spectrometer as a KBr pellet, and as neat samples on a Jasco FT/IR-4100 fitted with a Pike Miracle ATR device. UV/VIS spectra were recorded on a Perkin Elmer Lambda 19 spectrometer in diffuse reflectance mode with a $BaSO_4$ matrix. EDX was performed on an FEI XI 30 E7 environmental SEM.

Synthesis of $Co_{12}(OH)_{18}(ox)_3$(pip) (1).

Cobalt hydroxide (100 mg, 1.07 mmol), [pipH_2][ox$H$]$_2$ (71 mg, 0.27 mmol) and H_2O (8 ml) were heated in a 23 ml capacity Teflon-lined autoclave (Parr) to 225 °C under autogenous pressure for 12 hours. After cooling, the product is obtained as a blue, microcrystalline solid, with a hexagonal prismatic morphology. The product was physically separated from a small amount of solid $Co_2(OH)_2(ox)$[21] through differences in 'bouyancy' in the components of the mixture in an upwards liquid flow. Specifically the mixture was placed in a glass tube with and upwards flow of water. The flow rate is adjusted until the downward force of gravity on one type of crystal components of the mixture is countered by the force of the flowing fluid. With our product rising and the impurity sinking. The recovered product was collected by fltration and air dried. Yield 115 mg (95 % by Co).

Found: C 8.97, H 1.99, N 1.92 %. Expected: C 8.81, H 2.07, N 2.05 %. IR (KBr, $\bar{\nu}$, cm^{-1}) 3626 m, 3589 m, 3555 m, 3231 m, 3138 w, 3056 w, 2980 w, 2921 w, 1891 w, 1655 m, 1603 s, 1443 m, 1385 m, 1362 m, 1314 s, 1268 m, 1102 m, 1089 m, 1021 m, 994 m, 840 m, 803 s, 743 s, 609 s, 493 s, 463 s [Fig. S7 in ESI]. UV ($BaSO_4$, diffuse reflectance, cm^{-1}) 15900 $^4A_2 \rightarrow {}^4T_1$(P) tetrahedral, 16900 (tetrahedral doublet excited state), 21700 $^4T_{1g}$(F) $\rightarrow {}^4T_{1g}$(P), 40000 oxalate absorption.

Synthesis of 2.

The synthesis of **2** was performed under similar conditions to that described for **3** (see below). However in the synthesis of **2**, NaBr and $Na_2(ox)$ were used in place of KBr and $K_2(ox)(H_2O)$. The synthesis of **2** is less efficient than the corresponding synthesis of **3**, and only very small quantities of fine blue hexagonal crystal were produced amongst much larger quantities of recrystallised NaBr and $Na_2Co_2(ox)_3(H_2O)_2$.[23] The characterisation of **2** was limited to single crystal diffraction studies.

Synthesis of 3.

$CoCl_2(H_2O)_6$ (203 mg, 0.853 mmol), $K_2(ox)(H_2O)$ (0.311 mg, 1.69 mmol), KBr (16.04 g, 134 mmol) and H_2O (5.0 ml, 278 mmol) were placed in a 23 ml capacity Teflon lined autoclave and heated to 235 °C under autogenious pressure for 4 hours and allowed to cool slowly back to room temperature over 10 hours. Both KBr and the chain compound[24] $K_2Co(ox)_2$ crystallise out as the major solid components. Optical microscopy reveals two additional materials; black cobalt oxide, and thin blue triangular plates of **3**. The yield of both of these phases is quite variable, and never greater than 1% of the solid produced. Purification of **3** is achieved treating the reaction mixture with an excess distilled water, KBr is dissolved and $K_2Co(ox)_2$ decomposes producing a fine precipitate of $Co(ox)(H_2O)_2$. Sonication of the reaction mixture (**3**, $Co(ox)(H_2O)_2$, H_2O) in a boiling tube provides a suspension, out of which the product **3** settles much more quickly than the impurities, which can then be removed by decanting. Addition of more water, and repetition of this process yields a small sample of **3**. Optical microscopy shows an apparently pure and homogeneous product. This homogeneity in shape and size and composition of the crystallites that make up the product is also seen in the SEM and EDX measurements.

IR (ATR, $\bar{\nu}$ cm^{-1}) 3515 (m), 3469 (m), 3401 (m), 3326 (m), 1625 (s), 1360 (m), 1316 (m), 940 (w), 905 (w), 779 (m), 732 (m), 639 (s) [Fig. S7 in ESI].

EDX: 252 kV atom(excitation), O(K) 58, Br(L) 3.0, Cl(K) 0.86, K(K) 2.2, Co(K) 36 atom %.

X-ray Crystallography

Data for all structures were collected on an Enraf Nonius Kappa CCD using Mo-$K\alpha$ radiation, as ϕ scans and ω scans to fill the Ewald sphere. Data collection, cell

refinement and data reduction were carried out using COLLECT[32] and DENZO.[33] The structure solutions were obtained by direct methods (SHELXS-97 [34]) and a full-matrix least-squares refinement on F^2 was performed on all reflections by SHELXL-97[34] in the WINGX environment.[35] In view of the limited data quality obtained from these very small, structurally anisotropic crystals, a number or chemically sensible restraints and constraints were applied.

Crystallographic data (excluding structure factors) have been deposited with the Cambridge Crystallographic Data Centre as supplementary publications CCDC 275122 (**1**), CCDC (**2**) 275671 and CCDC 219800 (**3**). Copies of the data can be obtained free of charge on application to CCDC, 12 Union Road, Cambridge, CB2 1EZ, UK (Fax: +44 (0) 1223-336-033; E-mail: deposit@ccdc.cam.ac.uk).

Refinement details for 1.

Only cobalt atoms were refined anisotropically while all other non-H atoms were refined isotropically. The atoms C(2A) and C(2B) from the piperazine had their thermal parameter constrained to be equal, as did the three independent atoms of the oxalate anion; O(4), O(5) and C(1). All C-C and C-N bond distances in the piperazine were restrained to ideal values. All H atoms were placed in ideal geometries with thermal parameters fixed at $1.2 \times U_{iso}$ the parent atom and refined in riding mode.

General refinement details for 2 and 3.

A number of restraints and constraints were applied in order to best resolve this complex and partially disordered structure. While the thermal parameters of similar groups of atoms were constrained to the same values, the two structures were treated slightly differently due to differences in data quality. The better quality data for **2**, allows a meaningful refinement of more model parameters than could be achieved for **3**. Otherwise both structural models were very similar and subject to many of the same restraints and constraints. All H atoms were placed in idealized geometries, with occupancies equal to that of the parent atoms, isotropic thermal parameters fixed at $1.2 \times U_{iso}$ of the parent atom and then refined in riding mode. Only the H atoms on the water molecules, and on the hydroxyl O(24) were not included in the model due to the ambiguity in their positions. The occupancies of Co(8) and Co(8A)/Co(8B) were constrained to sum to 100 %. The partially occupied water; sites O(27) and O(28)

were placed in idealized geometries, on the apical site of the tetrahedrally coordinated cobalt ions (Co(8A) and Co(8B)) and refined in riding mode. The occupancies of all bromide ions, and the hydroxyl group (O(24)) were constrained by the Co(8) – Co(8A)/Co(8B) disorder, to preserve electroneutrality.

Specific refinement details for 2.

All Co atoms were refined with anisotropic thermal parameters, except the partially occupied sites Co(8A) and Co(8B), for which a single isotropic thermal parameter was refined. The anisotropic thermal parameters of the tetrahedral ions Co(3) and Co(7) were constrained to be equal. The atoms of the oxalate anions had their thermal parameter constrained to be equal, as did all the oxygen atoms from hydroxyl groups. The oxygen atoms; O(25) and O(26) (water of crystallisation) had their isotropic thermal parameters refined freely.

Specific refinement details for 3.

All K, Br and Co atoms had their isotropic thermal parameters refined freely, except the tetrahedrally coordinated cobalt atoms; Co(3), Co(7), Co(8A), Co(8B), which were constrained to be identical. All atoms in the oxalate and hydroxyl anions, and water (coordinated to Co) were constrained with the same isotropic thermal parameter. The oxygen atoms; O(25) and O(26) (water of crystallisation) had their isotropic thermal parameters refined freely.

Magnetic characterisation.

All magnetic measurements were performed a Quantum Design MPMS SQUID magnetometer with polycrystalline samples of **1** and **3**. Both samples were embedded in eicosane and held in a gelatine capsule to prevent reorientation effects. A diamagnetic correction was estimated from Pascal's constants[36] (χ_{dia} for **1** = -42.0×10^{-6} cm^3 mol^{-1} (per Co)). Static (dc) measurements were performed between 2 - 290 K in several applied field using a FCM protocol. Initial magnetisation curves were obtained from samples that were cooled in H = 0 G, and then the field swept up to 55 kG for a range of temperatures. Hysteresis curves were obtained between ±55 kG.

Dynamic (ac) measurements were performed using a oscillating field amplitude of 3.5 G and a frequency of 103 Hz, an H_{dc} offset field was varied between 0 - 800 G.

Acknowledgments

We are grateful to the EPSRC of the UK for the award of and Advanced Research Fellowship to DJP and for the funding crystallographic facilities.

References

[1] C. Sanchez, B. Julián, P. Belleville, M. Popall, *J. Mater. Chem*., 2005, **15**, 3559–3592; D.J. Chesnut, D. Hagrman, P.J. Zapf, R.P. Hammond, R. LaDuca Jr., R.C. Haushalter, J. Zubieta, *Coord. Chem. Rev*., 1999, **190-192**, 737-769.

[2] A.J. Fletcher, K.M. Thomas, M.J. Rosseinsky, *J. Solid State Chem.*, 2005, **178**, 2491–2510; J.Y. Lee, O.K. Farha, J. Roberts, K.A. Scheidt, S.T. Nguyen and J.T. Hupp*, Chem. Soc. Rev*., 2009, **38**, 1450-1459.

[3] L. J. de Jongh, A. R. Miedema, *Adv. Phys*., 2001, **50**, 947–1170.

[4] *Magnetic Properties of Layered Transition Metal Compounds*, L.J. de Jongh (Ed.), Kluwer Academic Publishers, Dordrect, 1989.

[5] M. Ogawa, S. Asai, *Chem. Mater*., 2000, **12**, 3253-3233; G. R. Williams, T.G. Dunbar, A.J. Beer, A.M. Fogg, D. O'Hare, *J. Mater. Chem*., 2006, **16**, 1222-1230; G. R. Williams, T.G. Dunbar, A.J. Beer, A.M. Fogg, D. O'Hare, *J. Mater. Chem*., 2006, **16**, 1231-1237.

[6] N. Chakroune, G. Viau, S. Ammar, N. Jouini, P. Gredin, M.J. Vaulay, F. Fiévet, *New J. Chem*., 2005, **29**, 355-361.

[7] P. Boulet, H.C. Greenwell, S. Stackhouse, P.V. Coveney, *J. Mol. Struct.-Theochem.*, 2006, **762**, 33-48.

[8] M. Bellotto, B. Rebours, O. Clause, J. Lynch, D. Bazin, E. Elkaïm, *J. Phys. Chem*. 1996, **100**, 8527-8534.

[9] P. Beaudot, M.E. De Roy, J.P. Besse, *Chem. Mater*., 2004, **16**, 935-945; M. del Arco, S. Cutiérrez, C. Martin, L. Rives, *Inorg. Chem*., 2003, **42**, 4232-4240.

[10] L.A. Groat, *Am. Mineral*., 1996, **81**, 238-243.

[11] R. Vonhodenberg, W. Krause, G. Schnorrerkohler, H. Tauber, *Neues Jahrb. Mineral. Monatsh.,* 1985, 550-556.

[12] M. Kurmoo, *Chem. Mater*., 1999, **11**, 3370-3378.

[13] M. Kurmoo, H. Kumagai, S.M. Hughes, C.J. Kepert, *Inorg. Chem.,* 2003, **42**, 6709-6722.

[14] R. Ma, Z. Liu, K. Takada, K. Fukuda, Y. Ebina, Y. Bando, T. Sasaki, *Inorg. Chem*., 2006, **45**, 3964-3969.

[15] P.M. Forster, M.M. Tafoya, A.K. Cheetham, *J. Phys. Chem. Solid*, 2004, **65**, 11-16.

[16] A. Rujiwatra, C.J. Kepert, J.B. Claridge, M.J. Rosseinsky, H. Kumagai, M. Kurmoo, *J. Am. Chem. Soc.,* 2001, **123**, 10584-10594.

[17] X.-M. Zhang, X.-H. Zhang, H.-S. Wu, M.-L. Tong, S.W. Ng, *Inorg. Chem*., 2008, **47**, 7462-7464.

[18] R. Moessner, A. P. Ramirez, *Physics Today*, Feb 2006, 24-29; A.P. Ramirez, *Annu. Rev. Mater. Sci*., 1994, **24**, 453-480; J.E. Greedan, *J. Mater. Chem*., 2001, **1**, 37-53; A. Harrison, *J. Phys. Condens. Mater.,* 2004, **10**, S553-S572.

[19] J.C. Hudson, *Prof. Geogr*. 1967, **19**, 133-135.

[20] E. Stryjewski, N. Giodrano, *Adv. Phys*., 1977, **26**, 487-650.

[21] D.J. Price, F. Lionti, R. Ballou, P.T. Wood, A.K. Powell, *Phil. Trans. Proc. Roy. Soc. A*, 1999, **357**, 3089-3118.

[22] R.-K. Chiang, C.-C. Huang, C.-S. Wur, *Inorg. Chem*., 2001, **40**, 3237–3239; T.D. Keene, M.B. Hursthouse, D.J. Price, *New J. Chem*., 2004, **28**, 558-561.

[23] D.J. Price, A.K. Powell, P.T. Wood, *J. Chem. Soc., Dalton Trans.,* 2000, 3566-3569.

[24] M.B. Hursthouse, M.E. Light, D.J. Price, *Angew. Chem. Int. Ed.*, 2004, **43**, 472–475.

[25] Y.-Q. Sun, J. Zhang, G.-Y. Yang, *Dalton Trans*., 2003, 3634 –3638.

[26] S. Natarajan, *Solid State Sci*., 2002, **4**, 1331-1342.

[27] F.H. Allen, *Acta Cryst*. 2002, **B58**, 380-388.

[28] Ch. Mockenhaupt, Th. Zeiske, H.D. Lutz*, J. Mol. Struct*., 1998, **443**, 191-198.

[29] D. Schmalfu, P. Tomczak, J. Schulenburg, J. Richter, *Phys. Rev. B*, 2002, **65**, 224405.

[30] D.J. Price, A.K. Powell, P.T. Wood*, Dalton Trans*., 2003, 2478–2482; C. Mennerich, .H.-H. Klauss, A.U.B. Wolter, S. Süllow, F.J. Litterst, C. Golze, R. Klingeler, V. Kataev, B. Büchner, M. Goiran, H. Rakoto, J.-M. Broto, O. Kataeva, D.J. Price, *Quantum Magnetism; NATO Science for Peace and Security Series B - Physics and Biophysics.* 2008 (Springer, Dordrecht) Eds, B Barbara, Y. Imty, G Sawatzky, P.C.E. Stamp, pages 97–124; T.D. Keene, I. Zimmermann, A. Neels, O. Sereda, J. Hauser, M. Bonin, M.B. Hursthouse, D.J. Price, S. Decurtins, *Dalton*

Trans., 2010, **39**, 4937-4950; T.D. Keene, M.B. Hursthouse, D.J. Price, *Cryst. Growth Design*, 2009, **9**, 2604-2609.

[31] R. Vaidhyanathan, S. Natarajan, C.N.R. Rao, *J. Chem. Soc., Dalton Trans*., **2001**, 669-706.

[32] R.W.W. Hooft 1998, COLLECT, Nonius BV, Delft, Netherlands.

[33] Z. Otwinowski, W. Minor, *Methods in Enzymology* (1997) Vol. **276**: *Macromolecular Crystallography*, part A, pp. 307−326; C. W. Carter, Jr., R. M. Sweet, Eds., Academic Press.

[34] G. M. Sheldrick, *Acta Cryst*. 1990, **A46**, 467−473.

[35] L.J. Farrugia, *J. Appl. Crystallogr*., **1999**, *32*, 837-838.

[36] *Magnetochemistry* R. L. Carlin, 1986, Springer-Verlag, Heidelberg.

Table 1: Crystallographic data

Compound	**1**	**2**	**3**
Idealised Formula	$Co_{12}C_{10}H_{28}N_2O_{30}$	$NaCo_{28}Br_2C_{12}H_{45}O_{68}$	$KCo_{28}Br_2C_{12}H_{45}O_{68}$
Crystal shape	blue plate	blue plate	blue plate
Crystal size /mm	$0.08 \times 0.08 \times 0.01$	$0.20 \times 0.10 \times 0.01$	$0.03 \times 0.03 \times 0.001$
Crystal system	trigonal	trigonal	trigonal
Space group	$P\bar{3}$	$P31c$	$P31c$
a/ Å	9.420(2)	13.7854(4)	13.8140(1)
c/ Å	10.242(4)	19.7548(9)	19.9012(2)
V/ Å^3	787.1(4)	3251.2(2)	3288.88(6)
Z	2	2	2
ρ_{calc}/g cm^{-3}	2.877	3.242	3.194
$2\theta_{max}$/ °	55.08	55.00	41.22
μ/ mm^{-1}	6.259	8.465	8.272
T/ K	120(2)	150(2)	120(2)
Refl. collect.	3998	13734	15832
Refl. unique	1180	4568	2233
R_{int}	0.2249	0.0889	0.1217
Complet. to θ_{max}	97.0 %	99.5 %.	99.6 %
Obs. criterion	$I > 2\sigma(I)$	$I > 2\sigma(I)$	$I > 2\sigma(I)$
Obs. reflect.	567	3261	2160
Parameters	50	193	147
Restraints	7	2	3
R1 (2σ(I) data)	0.1209	0.0556	0.0405
R1 (all data)	0.2156	0.0896	0.0420
wR2 (2σ(I) data)	0.2786	0.1221	0.0990
wR2 (all data)	0.3334	0.1365	0.1003
S (all)	1.048	0.994	1.051
Flack parameter	n/a	0.07(3)	0.07(3)
Res. peak / eÅ^{-3}.	2.322	1.810	0.919
Res. hole / eÅ^{-3}.	–1.217	–1.018	–0.729
CCDC No.	275122	275671	219800

Table 2: Hydrogen bonding and other contacts in **1**.

D–H···A	D–H /Å	H···A /Å	D···A /Å	D–H–A /°
O(2)–H(2)···O(4)	0.98	2.28	3.108(21)	153
O(3)–H(3)···O(5)	0.98	2.04	2.977(20)	159
O(1)–H(1)···O(5)	0.98	2.65	3.573(19)	156
N(1)–H(4)···O(4)	0.91	3.24	4.130(14)	168

Table 3: Short contacts in **2** [and **3**] indicating significant hydrogen bonds

D–H···A	D–H /Å	H···A /Å	D···A /Å	D–H–A /°
O9–H9···Br1^{iv}	0.98 [1.00]	2.25 [2.23]	3.200(7) [3.198(7)]	164 [164]
O10–H10···O4	0.98 [1.00]	1.86 [1.85]	2.811(11) [2.815(11)]	163 [162]
O11–H11···Br1^{iv}	0.98 [1.00]	2.56 [2.53]	3.335(8) [3.323(8)]	137 [136]
O13–H13···O1	0.98 [1.00]	1.89 [1.89]	2.831(11) [2.857(11)]	161 [161]
O14–H14···O3	0.98 [1.00]	1.95 [1.97]	2.903(11) [2.936(12)]	163 [163]
O15–H15···Br2^{iii}	0.98 [1.00]	2.57 [2.47]	3.358(8) [3.269(8)]	138 [137]
O17–H17···O5^{ii}	0.98 [1.00]	1.92 [1.95]	2.870(11) [2.909(11)]	163 [161]
O20–H20···O8^{iv}	0.98 [1.00]	1.94 [1.98]	2.860(11) [2.929(10)]	155 [157]
O21–H21···O6^{ii}	0.98 [1.00]	2.00 [1.98]	2.910(11) [2.913(11)	153 [154]
O23–H23···Br2^{iii}	0.98 [1.00]	2.26 [2.24]	3.218(8) [3.201(7)]	165 [162]
O19–H19···O7	0.98 [1.00]	1.91 [1.92]	2.853(11) [2.890(11)]	161 [162]
O19–H19A···O7	0.98 [1.00]	1.97 [1.99]	2.853(11) [2.890(11)]	149 [148]
O16–H16···O2^{i}	0.98 [1.00]	2.02 [2.05]	2.944(11) [2.998(11)]	157 [157]
O16–H16A···O2^{i}	0.98 [1.00]	2.01 [2.05]	2.944(11) [2.998(11)]	158 [157]
O18–H18···O26	0.98 [1.00]	2.11 [2.05]	3.03(4) [2.97(3)]	155 [153]
O12–H12···O25	0.98 [1.00]	2.22 [2.17]	2.996(3) [2.96(3)]	135 [135]

iv) y, x, z–$^1/_2$, ii) 1–x+y, 1–x, z, iii) 1+x, y, z, i) 2–x, 1–x+y, z–$^1/_2$.

Figures

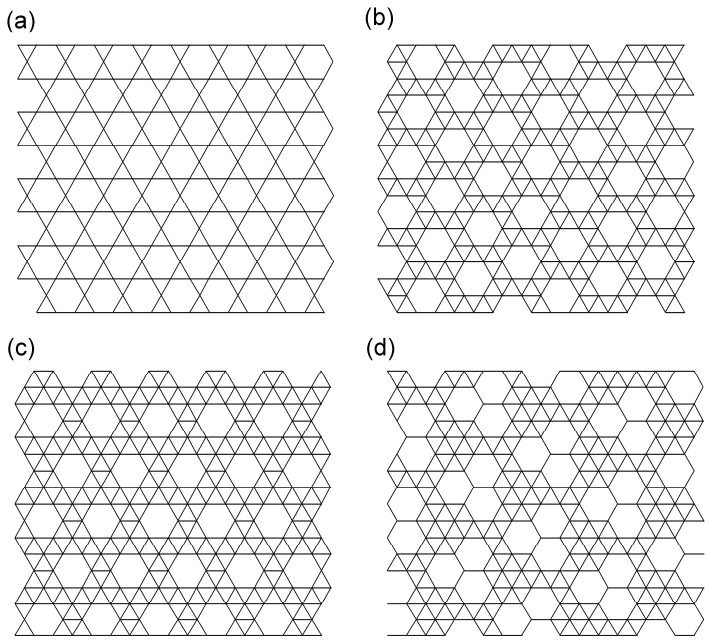

Fig. 1. Selected trigonally symmetric networks formed by site depletion of 2-D triangular lattices. **(a)** 1/4 depletion gives a semi-regular 3.6.3.6 net (the kagomé lattice), **(b)** 1/7 depletion give the semiregular 3.3.3.3.6 net, **(c)** 1/9 depletion, the network formed by octahedrally coordinated Co ions in **1**, **(d)** 3/19 depletion seen in the compound **2** and **3**.

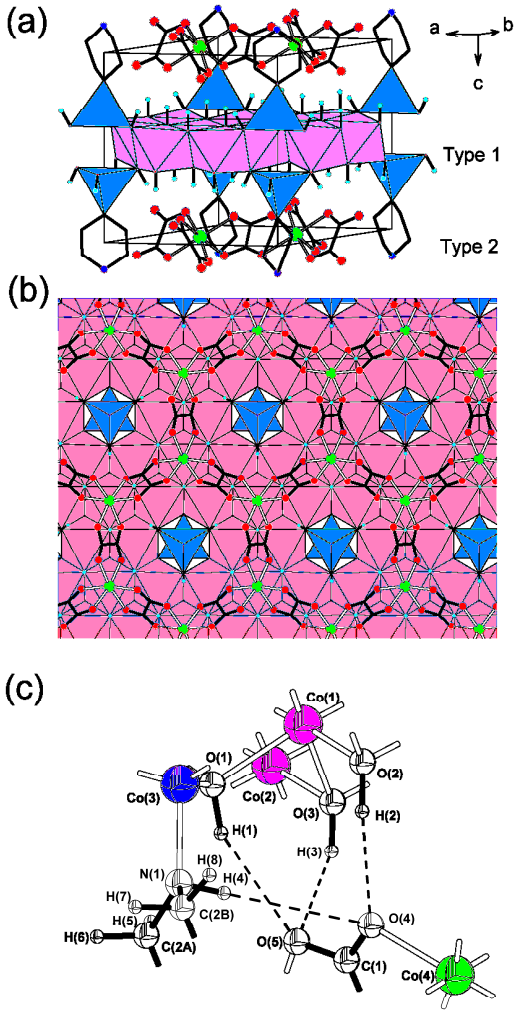

Fig. 2. The structure of **1**. **(a)** The crystallographic cell viewed roughly perpendicular to the *c*-axis showing the 2-D character to the material with an alternation of two types of layer. For clarity only a single orientation of piperazine is shown and some H-atoms are omitted. [Colour key: Co^{II} in coordination net - green, Co^{II} in hydroxide layer - pink (octahedral), blue (tetrahedral)]. **(b)** Viewed along the *c*-axis, showing the relationship between the coordination network and the metal hydroxide layers. **(c)** The asymmetric unit and atom labelling schemes for **1**. Showing the range of hydrogen-bonding interactions as discussed in the main text. In this structure Co(2), Co(3) and Co(4) all lie in three-fold axis, while the piperazine and oxalate ligands lie of inversion centres.

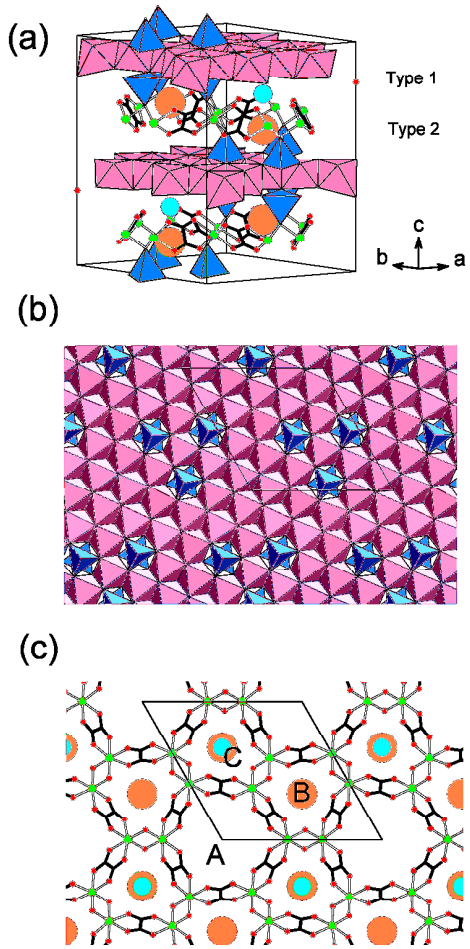

Fig. 3. Structure of **2** [and **3**]. **(a)** The unit cell of **2** [and **3**] viewed perpendicular to the *c*-axis, showing the layered character to the material. Layer types 1 and 2 are discussed in the text. [Colour key: Co^{II} in coordination net - green, Co^{II} in hydroxide layer - pink (octahedral), blue (tetrahedral), Br - orange, A = Na (K) - cyan]. **(b)** Layer type 1; a polyheadral representation of the decorated cobalt hydroxide layer in the *ab*-plane. **(c)** Layer type 2; showing the 2-D coordination network layer in the *ab*-plane, and the void spaces A, B and C which are described in the main text.

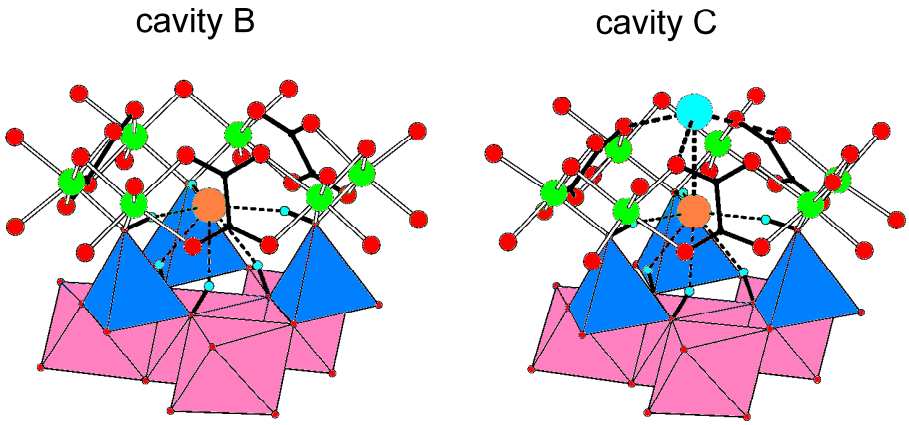

Fig. 4. The hydrogen bonded environment of the bromide ions in **2** [and **3**] found in the type B and C cavities. [Colour key: Co^{II} in coordination net - green, Co^{II} in hydroxide layer - pink (octahedral), blue (tetrahedral), Br - orange, Na [K] - cyan].

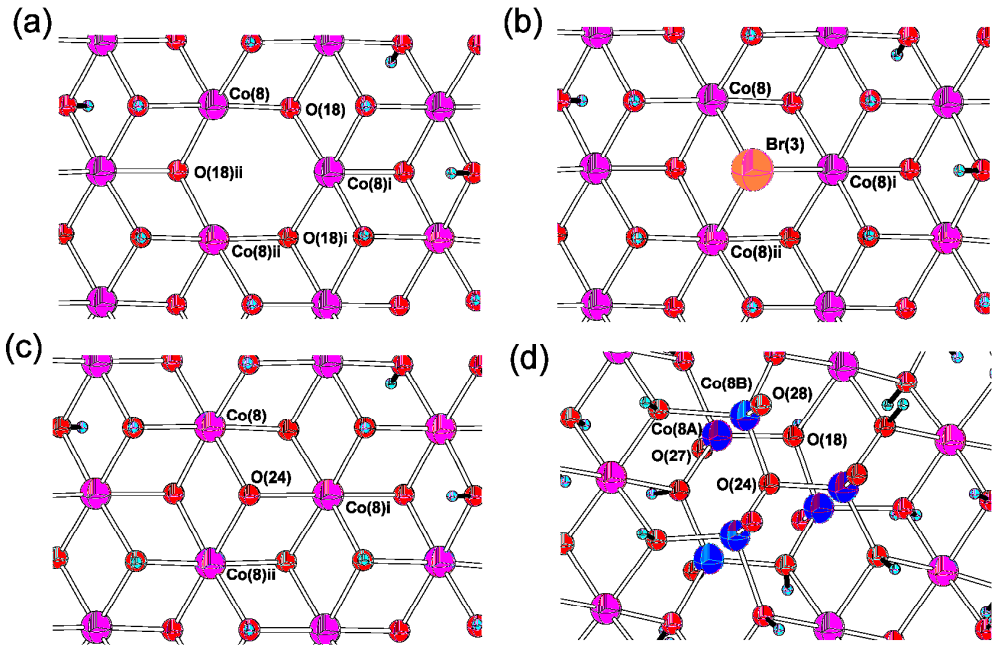

Fig. 5. Model of the disorder on the trigonally symmetric cavity, void A. Showing the different components to the overall structure. See text for details. The refined contributions to the structure of **2** [**3**] are determined as: **(a)** 29(3) % [35(2) %], **(b)** 25.6(14) % [19.4(14) %], **(c)** 35(3) % [35(2) %], **(d)** 10.2(3) % [6.0(2) %].

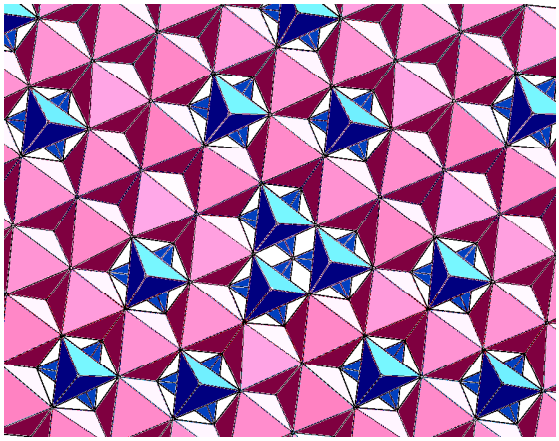

Fig. 6. Showing the two arrangements for the tetrahedrally coordinated Co(II) ions as a disordered component in void space A. On the underside we see the three tetrahedron sharing a common vertex, while on the top side we see a ring of three tetrahedrally coordinated ions.

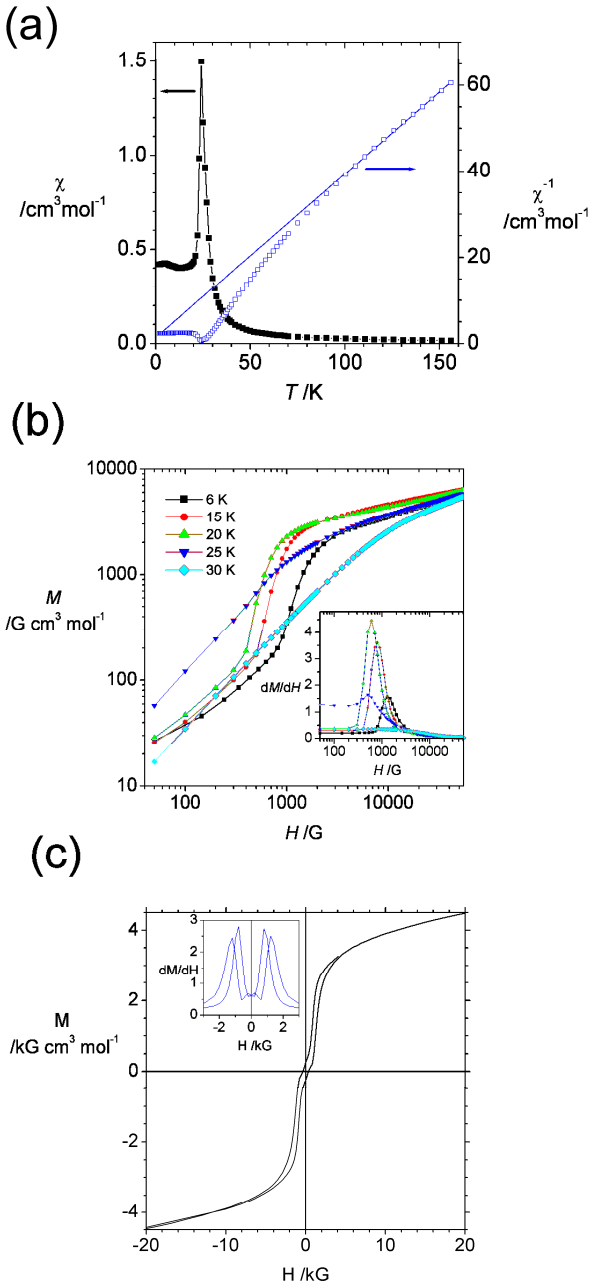

Fig. 7. Magnetic behaviour of **1**. **(a)** susceptibility and reciprocal susceptibility, showing abrupt magnetic phase transition. The best fit to Curie-Weiss law from the high temperature data is superimposed. Data derived from a FCM experiment (H = 200 G). **(b)** Initial magnetisation curves, determined by cooling the sample in zero field to a set temperatures then measuring the magnetisation as the field is swept. A field induced transition is apparent below T_c. The derivative curve is shown in the inset. **(c)** Hysteresis measurement at 6 K showing characteristic sigmoidal shape. The first derivative (susceptibility) is shown in the inset.

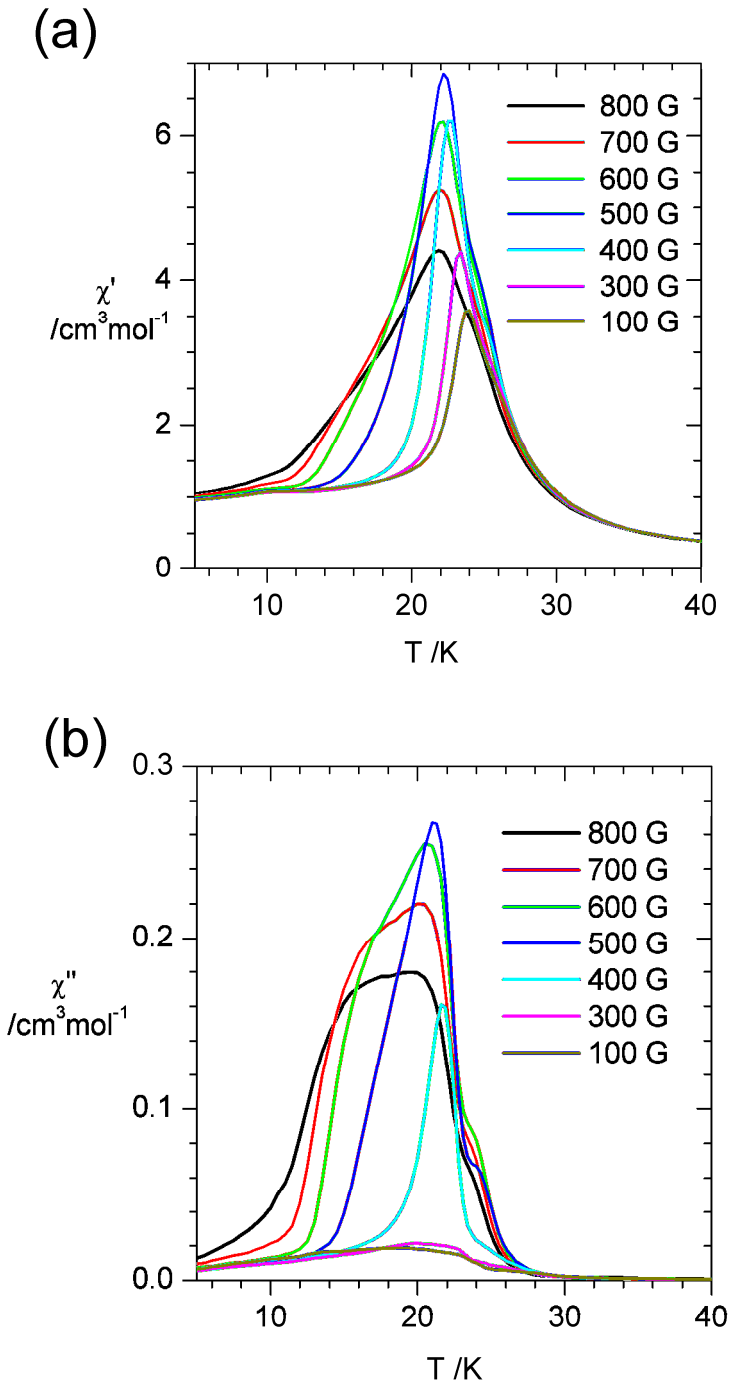

Fig. 8. Dynamic (a.c.) susceptibility of **1**, under a range of applied offset fields. **(a)** The thermal variation of the real component, $\chi'(T,\omega)$. **(b)** The variation in the out-of-phase, imaginary component, $\chi''(T,\omega)$.

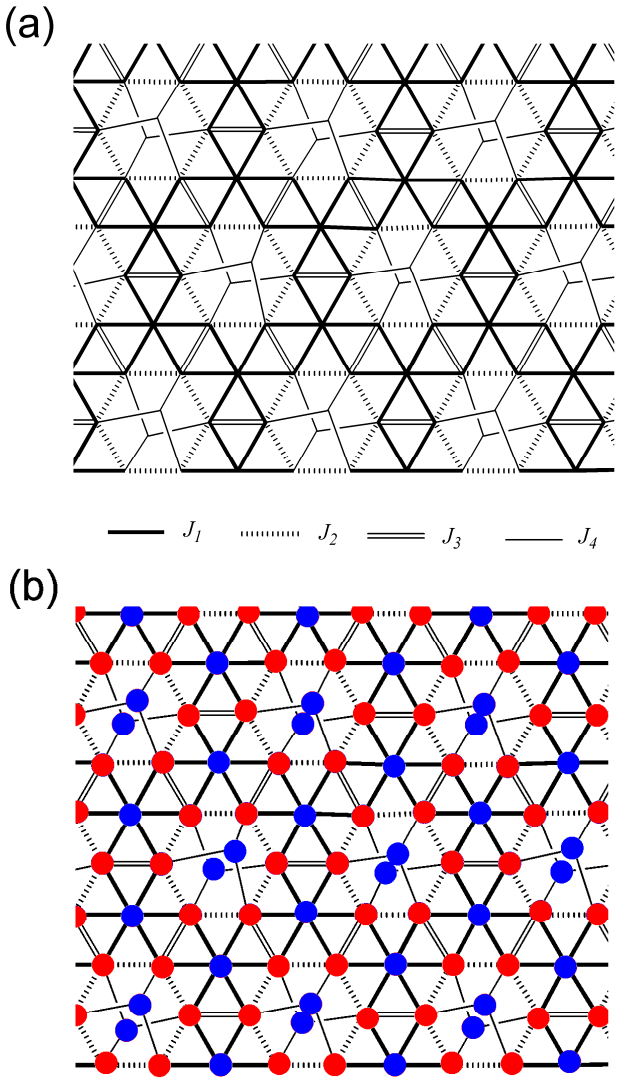

Fig. 9. (a) Coupling scheme within the type 1, hydroxyl layer in **1**. **(b)** A likely magnetic ground state (red spin up, blue spin down). The only non-frustrated (collinear) spin configuration with an expected saturation magnetisation close to the observed value.

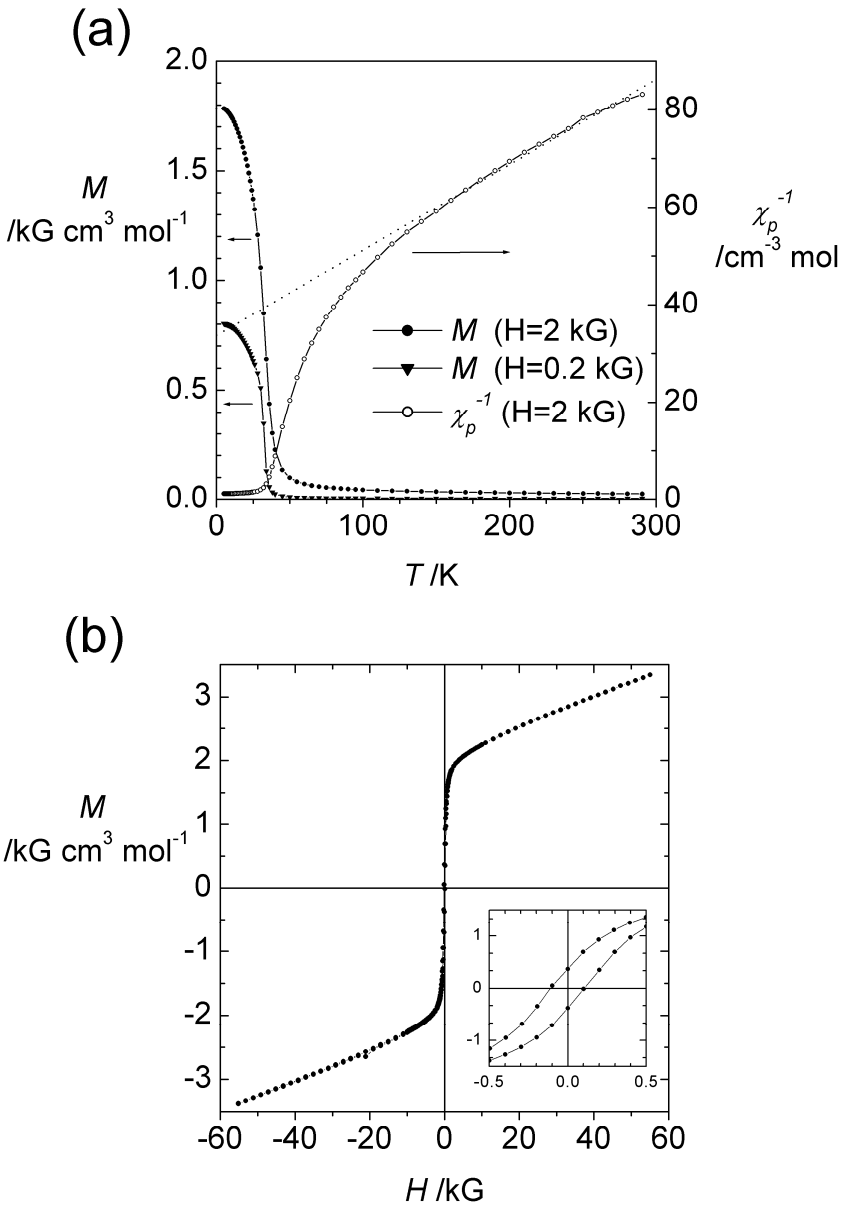

Fig. 10. (a) The magnetisation of **3** (at 0.2 and 2.0 kG) and the derived reciprocal susceptibility (at 2.0 kG) showing the fit to the high temperature Curie-Weiss behaviour. **(b)** The hysteresis of **3** at 10 K. The insert shows an expansion of the central region showing remnant magnetisation and coercive fields.